ACS APPLIED MATERIALS & INTERFACES

www.acsami.org

Research Article

Biorenewable Exfoliation of Electronic-Grade Printable Graphene Using Carboxylated Cellulose Nanocrystals

Janan Hui,[†] Haoyang You,[†] Anton Van Beek, Jinrui Zhang, Arash Elahi, Julia R. Downing, Lindsay E. Chaney, DoKyoung Lee, Elizabeth A. Ainsworth, Santanu Chaudhuri, Jennifer B. Dunn, Wei Chen, Stuart J. Rowan, and Mark C. Hersam*

Cite This: *ACS Appl. Mater. Interfaces* 2024, 16, 57534–57543

Read Online

ACCESS | Metrics & More | Article Recommendations | Supporting Information

ABSTRACT: The absence of scalable and environmentally sustainable methods for producing electronic-grade graphene nanoplatelets remains a barrier to the industrial-scale application of graphene in printed electronics and conductive composites. To address this unmet need, here we report the utilization of carboxylated cellulose nanocrystals (CNCs) extracted from the perennial tall grass *Miscanthus* × *giganteus* as a biorenewable dispersant for the aqueous liquid-phase exfoliation of few-layer graphene nanoplatelets. This CNC-based exfoliation procedure was optimized using a Bayesian machine learning model, resulting in a significant graphite-to-graphene conversion yield of 13.4% and a percolating graphene thin-film electrical conductivity of 3.4×10^4 S m^{-1}. The as-exfoliated graphene dispersions were directly formulated into an aerosol jet printing ink using cellulose-based additives to achieve high-resolution printing (~20 μm line width). Life cycle assessment of this CNC-based exfoliation method showed substantial improvements for fossil fuel consumption, greenhouse gas emissions, and water consumption compared to incumbent liquid-phase exfoliation methods for electronic-grade graphene nanoplatelets. Mechanistically, potential mean force calculations from molecular dynamics simulations reveal that the high exfoliation yield can be traced back to the favorable surface interactions between CNCs and graphene. Ultimately, the use of biorenewable CNCs for liquid-phase exfoliation will accelerate the scalable and eco-friendly manufacturing of graphene for electronically conductive applications.

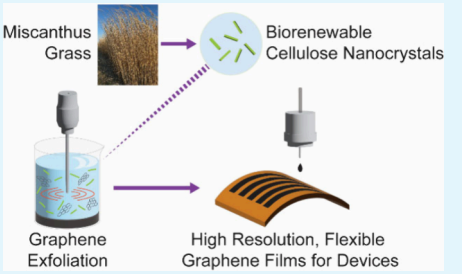

KEYWORDS: *cellulose nanocrystals, graphene, liquid-phase exfoliation, printed electronics, aerosol jet printing, Bayesian optimization, life cycle assessment*

1. INTRODUCTION

Graphene has attracted significant attention for next-generation printed electronics due to its high electrical conductivity, thermal conductivity, chemical stability, and mechanical resilience.[1,2] Despite broad applications spanning the fields of energy storage,[3,4] sensors,[5,6] and wearable devices,[7] industrial-scale manufacturing of graphene has been hampered by limited scalability and negative environmental impacts,[8,9] particularly when incorporated into electronically conductive inks for printed electronics.[10] Among the different production methods for graphene nanoplatelets, liquid-phase exfoliation (LPE) of graphite is widely considered to be the most scalable due to its simplicity, high throughput, and solution processability.[11,12] However, LPE methods often suffer from low graphite-to-graphene conversion yield and rely on non-renewable dispersants and/or hazardous solvents.[13,14] To minimize the environmental impact of LPE graphene production, renewable dispersants are required that can achieve high exfoliation yield using eco-friendly solvents.

Dispersants or stabilizers, such as polymers or surfactants additives, can aid shear exfoliation through interfacial interactions ($\pi-\pi$, cation$-\pi$, etc.) and weaken the $\pi-\pi$ stacking interactions between layers of graphene.[15] These dispersants further prevent the resulting graphene nanosheets from reaggregating, thereby improving the long-term stability of the colloidal suspension.[16] The chosen solvent medium and downstream purification requirements are generally determined by the solubility of the dispersant, which are all substantial contributors to environmental costs for an industrially scaled production system.[12] Typical combinations of dispersant and solvent include ethyl cellulose (EC) in ethanol,[17] and surfactants such as sodium cholate,[18,19] sodium deoxycholate,[20] Tween 80,[21] or Triton X-100 in *N*-methyl-2-pyrrolidone or water.[22] In particular, exfoliation with EC has demonstrated high-conductivity printed graphene films (5×10^4 S m^{-1}), but EC has limited solvent compatibility (i.e., only organic solvents) and results in low graphite-to-graphene conversion yields of ~1%.[17,23] Aqueous surfactant systems are

Received: July 28, 2024
Revised: September 26, 2024
Accepted: October 2, 2024
Published: October 11, 2024

https://doi.org/10.1021/acsami.4c12664
ACS Appl. Mater. Interfaces 2024, 16, 57534–57543

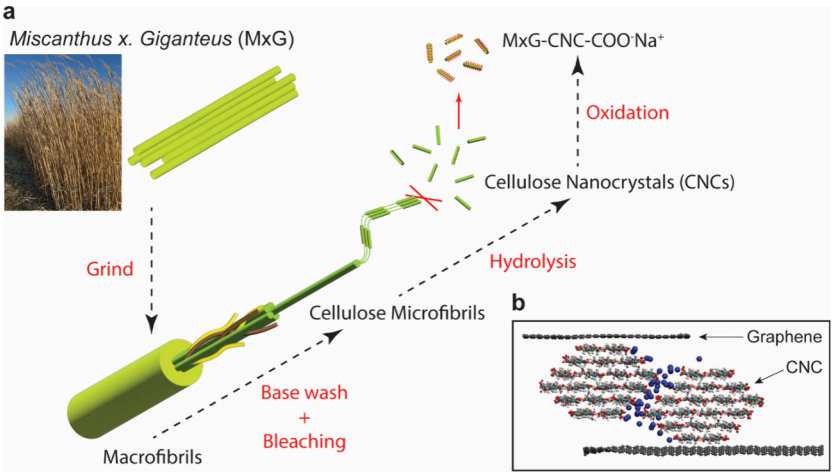

Figure 1. CNC extraction scheme and exfoliation visualization. (a) Processing schematic for the isolation of cellulose nanocrystals from MxG, depicting the grinding, base wash and bleaching, hydrolysis, and oxidation steps to form MxG-CNC−COO^-Na^+ that is used for exfoliation of graphene. (b) Visualization from a molecular dynamics simulation depicting bulk CNC crystals assisting with exfoliation between layers of graphene. The red, cyan, and white colors denote the oxygen, carbon, and hydrogen atoms of the CNC−COO^-, respectively. The graphene carbon atoms and Na^+ ions are colored gray and blue, respectively.

preferable from the perspective of the eco-friendliness of water as a solvent, yet surfactants can be problematic in industrial-scale processes. Specifically, if the surfactant concentration exceeds its critical micelle concentration, air bubbles introduced from shearing forces can form a foam film that affects yield and processability of the dispersion.[24,25] Moreover, surfactant residues are difficult to remove from the final graphene product, which can limit downstream electronics applications.[19,26] Solvent-only approaches have also been explored for graphene LPE, but the absence of dispersants results in low exfoliation yield, limited electrical conductivity, poor colloidal stability, and/or requires environmentally unfriendly solvents.[27−30] Therefore, it remains of high interest to identify eco-friendly, biorenewable dispersants that can achieve high graphite-to-graphene conversion yields in aqueous solvent.

Cellulose nanocrystals (CNCs) are a promising biorenewable material that can be extracted from natural wood or other biomass fibers. The desirable properties of CNCs include high surface area, crystallinity, mechanical strength, and tailorable surface functional groups that facilitate their use in a variety of composite materials.[31,32] Sulfated CNCs have also been shown to be promising dispersants or stabilizers for graphene in aqueous solution.[14,25,33,34] It has been theorized that the crystallinity and amphiphilic nature of the CNC structure plays a key role in graphene intercalation and stabilization.[25,35] Consistent with the cellulose I β crystal structure, CNCs have two hydrophobic (100) faces and four (110) or (1−10) hydrophilic faces.[36] On the (110) faces, each repeating unit of the cellulose chain has one primary alcohol on the C6 position of the glucose unit and two secondary alcohols on the C2 and C3 positions facing outward.[37,38] For carboxylated or sulfated CNCs, the (100) face is believed to favorably adsorb onto the surfaces of graphite layers, resulting in outward facing (110) surfaces with negatively charged surface groups that electrostatic repel each other to enhance exfoliation and subsequent colloidal stability of graphene.[14,25] Recently, graphene exfoliated with CNCs have even demonstrated biocompatibility with photosynthetic microorganisms, which has been exploited for low-cost biophotovoltaic devices.[25] CNCs as a dispersant would thus have minimal concern as an end-of-life pollutant, providing a pathway toward developing electronics with biodegradable, non-toxic waste. However, graphene−CNC films and composites have not demonstrated electrical conductivity above 10^3 S m^{-1}, and high-yield exfoliation conditions have not been identified. In addition to insufficient electrical conductivity, graphene−CNCs have not been applied in printed electronics due to poor printability of graphene−CNC dispersions and challenges in removing CNCs from printed graphene films.

Overcoming these limitations, here we report CNCs derived from the perennial tall grass *Miscanthus* × *giganteus* (MxG) as a biorenewable dispersant to achieve electronic-grade graphene nanoplatelets. A Bayesian machine learning model is utilized to identify exfoliation conditions that concurrently maximize the graphite-to-graphene conversion yield and thin-film electrical conductivity. The exfoliated graphene−CNC aqueous dispersion is then directly formulated into an aqueous-based aerosol jet printing ink with cellulose-based additives. This work thus achieves drop-on-demand printing of graphene exfoliated with fully biorenewable solvents and additives. Importantly, the printed films possess superlative electrical conductivity exceeding 10^4 S m^{-1} and printed spatial resolution down to 20 μm line width. Life cycle assessment quantitatively confirms that our eco-friendly graphene inks require 60−80% reduced fossil fuel usage, water consumption, and greenhouse gas (GHG) emissions compared to other LPE graphene inks. Overall, this work establishes a scalable eco-manufacturing pathway to electronic-grade printable graphene inks.

2. MATERIALS AND METHODS

2.1. Materials. Graphite flakes (3061 grade) were purchased from Asbury Graphite. MxG stalks were harvested at the University of Illinois at Urbana−Champaign. Sodium hydroxide (NaOH), acetic acid, sodium hypochlorite (NaOCl) solution (available chlorine 10−15%), Si/SiO_2 wafer (300 nm thermal oxide), and glass slides were purchased from Fisher Scientific. Poly-L-lysine solution was purchased from Ted Pella. Ethanol (200 proof) was manufactured by Decon Laboratories (King of Prussia, PA, U.S.A.) and purchased from Fisher Scientific (Waltham, MA, U.S.A., Catalog Number 04-355-223). Polyimide films (125 μm thick) were purchased from DuPont

https://doi.org/10.1021/acsami.4c12664
ACS Appl. Mater. Interfaces 2024, 16, 57534−57543

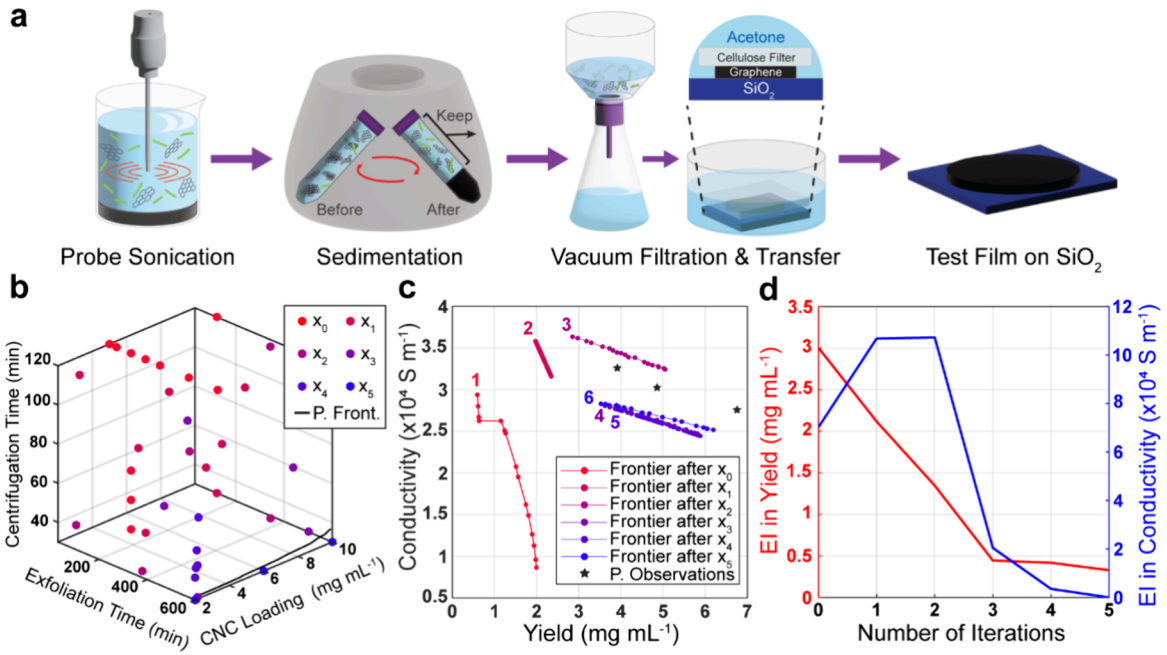

Figure 2. Bayesian optimization of graphene−CNC exfoliation processing. (a) Experimental workflow schematic depicting exfoliation, centrifugation, and test film formation used in optimization. (b) One-variable-at-a-time (OVAT) optimization sampled points (n = 11) and all five iterations of Bayesian sampled points (n = 26) plotted in the three-variable phase space (x_0−x_5). The final Pareto frontier after optimization (P. Front.) is highlighted in black. (c) Evolution of modeled Pareto frontiers after each Bayesian iteration in terms of electrical conductivity of vacuum-filtered films and graphene exfoliation yield. The final experimental results are highlighted as black stars (P. Observations). (d) Expected improvement (EI) curves for graphene exfoliation yield (red) and electrical conductivity of vacuum-filtered films (blue) over each Bayesian iteration.

Kapton. Cyrene, 3-aminopropyl triethoxysilane (99%), 2-propanol, concentrated hydrochloric acid (HCl), sodium chlorite ($NaClO_2$), 2,2,6,6-tetramethylpiperidine 1-oxyl (TEMPO), and sodium bromide (NaBr) were purchased from Sigma-Aldrich.

2.2. Extraction of Cellulose Nanocrystals. MxG-CNCs were isolated from MxG stalks according to a previously published procedure with some modifications (Figure 1).[39] MxG stalks were ground and washed with NaOH solution, bleached with $NaClO_2$ solution, and hydrolyzed with HCl to isolate crystalline subunit CNCs with alcohol groups on the C6 position in the glucose structure. C6-OH was then oxidized to carboxylate group ($-COO^-$) using TEMPO−NaBr−NaClO oxidation. The resulting product was a cotton-like powder MxG-CNC−COO^-Na^+ with over 86% crystallinity, average length of 212 nm, average thickness of 3.2 nm, and a surface functionality of 2.1 mol kg^{-1} of $-COO^-Na^+$ groups. The full isolation procedure and detailed characterization of the CNCs can be found in Figure S2 of the Supporting Information.

2.3. Liquid-Phase Exfoliation of Graphene and Ink Formulation. Exfoliation of graphite flakes using MxG-CNC−COO^-Na^+ was adapted based on a previously published procedure,[33] but required further optimization due to the different surface functional groups (carboxylate instead of sulfate half ester groups). CNCs were first dispersed in deionized water at a concentration of 2−10 mg mL^{-1} using 10 min of probe sonication (Fisher Scientific Sonic Dismembrator Model 500, 13 mm Branson tip) in a stainless-steel beaker. Then, 50 mg mL^{-1} of natural graphite flakes were added and probe sonicated for 30−600 min to cause shearing into graphene nanosheets. A Julabo F250 recirculating chiller was used to maintain a constant temperature of 4 °C during the exfoliation process. This procedure led to a polydisperse mixture of graphite and graphene that required separation by centrifugation (Beckman Coulter Avanti J-26 XPI) at 4500 rpm (~3700g) for 30−120 min. Graphitic particles were sedimented to leave a supernatant containing exfoliated graphene−CNC. The resulting supernatant dispersions demonstrated high colloidal stability with no detectable sedimentation over a period of 6 months.

2.4. Vacuum Filtration and Film Transfer. Vacuum-filtered test films of graphene−CNC dispersions were prepared by filtering diluted supernatant (1 mg of graphene total) onto a mixed cellulose ester filter with 0.1 μm pores. This film was transferred onto a glass slide by dissolving the mixed cellulose ester filter in an acetone bath. The graphene−CNC film on the surface of the glass slide was subsequently annealed in a box furnace (BF51818C-1, Thermo Scientific) at 350 °C in air for 30 min to pyrolyze the cellulose nanocrystals and improve the electrical conductivity of films.

2.5. Aerosol Jet Printing. To achieve suitable rheological properties for aerosol jet printing (AJP), 5% (v/v) cyrene and 10% (v/v) ethanol was directly added to the aforementioned supernatant graphene−CNC dispersion followed by bath sonication for 10 min. The resulting ink was filtered through a 1.6 μm glass microfiber syringe filter (Whatman). Graphene−CNC films were aerosol jet printed (AJ200, Optomec) onto glass, Si/SiO_2 wafer, or polyimide substrates that were heated to 80 °C in air during printing. During the AJP process, the ink was atomized in an ultrasonication bath held at 30 °C by applying a current of ~0.5 mA. The resulting aerosolized ink was deposited with the aid of a nitrogen sheath flow and a nitrogen carrier flow. Sheath flow rates were in the range of 40−60 sccm, and carrier flow rates were in the range of 15−25 sccm. The printing speed was maintained at 1 mm s^{-1} for all 3 layers of printing for 4 × 3 mm films. Following printing, the devices were annealed in a box furnace at 350 °C in air for 30 min.

2.6. Life Cycle Assessment (LCA). LCA is a robust and holistic methodology to evaluate and compare the environmental impacts of similar products, which can be produced by different processes.[40,41] In this study, LCA was completed on the inputs of six different electronic-grade LPE graphene production methods, where electronic-grade is defined as a printable film with an electrical conductivity exceeding 10^4 S m^{-1}. The fossil energy usage, GHG emissions, and water consumption were calculated based on the functional unit of 1 g of graphene produced by each method.

2.7. Molecular Dynamics (MD) Simulations. MD simulations were used to compute the tendency of the TEMPO-oxidized CNCs

https://doi.org/10.1021/acsami.4c12664
ACS Appl. Mater. Interfaces 2024, 16, 57534−57543

(CNC−COO$^-$) to attach to graphene flakes or agglomerate based on the effects of carboxylation. CNC−COO$^-$ were built with I β crystal structure, which consists of 18 cellulose chains composed of 8 glucose units.[37] Graphene sheets were positionally restrained (fixed-graphene) in a 7.2 × 6.1 × 7.0 nm^3 box. See the Supporting Information for full details on the simulation setup and procedure. For graphene adsorption simulations, we calculated the potential mean force (PMF) of binding for free-CNC−COO$^-$ approaching a fixed graphene sheet for both hydrophilic (110) and hydrophobic (100) orientations of CNC−COO$^-$. For the repulsion simulations, free-CNC−COO$^-$ approached a constrained CNC−COO$^-$ (fixed-CNC−COO$^-$) through the hydrophobic−hydrophobic (100−100) and hydrophilic−hydrophilic (110−110) orientations. For all studied systems, binding partners were placed 1.7 nm apart in a simulation box filled with water, and Na^+ ions were added to neutralize the system. Then, we used a 120 000 kJ mol^{-1} nm^{-2} force constant to push the free-CNC−COO$^-$ toward the adsorbent in a 15 ns simulation, using a pushing rate of 0.0001 nm ps^{-1}. The pushing simulation generated the reaction coordinate for the umbrella sampling simulations and, accordingly, PMF calculations. Finally, we used the weighted histogram method to remove bias from the window simulations and construct the PMF profile of binding.[42] For the systems where the pushing simulations did not yield direct contact between the binding surfaces, we conducted pulling simulations between fixed and free CNC−COO$^-$ instead. In the pulling simulations, CNC−COO$^-$ or pristine CNCs (CNC−OH) were placed adjacent to each other and then pulled apart to generate the reaction coordinate for the PMF calculations.

3. RESULTS AND DISCUSSION

3.1. Optimization of Graphene−CNC Exfoliation Procedure. Carboxylated CNCs were obtained from MxG (Figure 1a) to explore their use in the biorenewable exfoliation of graphite. The nanoscale dimensions of the carboxylated CNCs (212 ± 75 nm length, 1.8 ± 0.4 nm height) intercalate between graphite layers with the inclusion of shear forces (Figure 1b), and the high crystallinity index (86%) suggests well-defined amphiphilic surfaces that can enhance exfoliation as discussed in previous work (Figure S1 of the Supporting Information).[25,33] Furthermore, the highly carboxylated surface of the CNCs (~2.1 mol kg^{-1}) allows dispersibility in water within 10 min of bath sonication, resulting in stable colloidal suspensions for concentrations up to 35 mg mL^{-1}. The CNCs were used to ultrasonically exfoliate graphite in aqueous media, with initial optimization using a one-variable-at-a-time (OVAT) approach to observe how different variables influence graphene exfoliation yield and electrical conductivity of vacuum-filtered test films (Figure 2a). Based on initial results and previous LPE studies, we found that CNC loading, exfoliation time, and centrifugation time contribute significantly to graphene exfoliation yield and film electrical conductivity.[43,44] The conditions of 5 mg mL^{-1} CNC loading, 240 min exfoliation time, and 120 min centrifugation time were found to achieve the best performance following OVAT optimization (Figure S2 of the Supporting Information), resulting in a graphene concentration of 0.77 mg mL^{-1} (~1.5 wt % yield) and an electrical conductivity of 1.9 × 10^4 S m^{-1}.

Despite the high electrical conductivity achieved, the OVAT approach does not fully explore the phase space of the three variables, nor does it optimize for both graphene exfoliation yield and electrical conductivity simultaneously. Consequently, we employed a Bayesian-based machine learning multivariable optimization method in an effort to efficiently identify superior processing conditions (Figure 2).[45] In this method, Gaussian process models are used to provide posterior predictive distributions of graphene exfoliation yield and electrical conductivity. Specifically, Gaussian processes have the advantage of quantifying the experimental uncertainty and prediction uncertainty that can be used for multivariable optimization with a limited number of experiments. We trained an initial Gaussian process using the initial experiments from the OVAT optimization that enabled the prediction of the graphene exfoliation yield and electrical conductivity for untested processing conditions. An acquisition function was then used to obtain new experimental sample points, which balances the testing of unexplored regions in the phase space and exploitative testing based on previously observed high performing conditions. New sample conditions were tested and added to the model with continued iteration until a stopping criterion was met. Specifically, experimentation was stopped once insignificant change in conditions for new sample points was observed. This search strategy guides the model toward a series of points on the Gaussian surface that have superior graphene exfoliation yield or electrical conductivity in at least one objective compared to all other points (named the Pareto frontier). As such, the Pareto frontier is a series of points that maximizes graphene exfoliation yield and electrical conductivity while minimizing the trade-off between them. Detailed discussion of the theory and design of the Bayesian optimization can be found in the Supporting Information. The completed model builds on the data from the original OVAT optimization and adds four iterations of 5−8 points for a total of 37 points explored in the designed variable phase space (Figure 2b). Exploration of the phase space was deemed sufficient based on the convergence of the Pareto frontier and insignificant expected improvement values after the last two iterations of Bayesian-chosen points (panels c and d of Figure 2).

Relationships between variables and responses were elucidated by the results of the model. Graphene exfoliation yield and electrical conductivity were both found to increase monotonically with exfoliation time until the instrumentation limit was reached at 600 min of exfoliation. At this limit, centrifugation time and CNC loading had minimal effect on electrical conductivity, but dramatically changed the graphene exfoliation yield. In particular, graphene exfoliation yield is maximized for high exfoliation times, excess CNC loading, and low centrifugation times. Specifically, longer exfoliation time and excess CNCs lead to more shearing and collisions to produce more graphene. Meanwhile, shorter centrifugation time sediments out less product to improve graphene exfoliation yield at the cost of a more polydisperse flake size. However, these extremes for optimizing graphene exfoliation yield also influences the quality of the resulting graphene flakes and thus their electrical conductivity in a film.

The graphene flake size distribution is a key factor in determining the electrical conductivity of a percolating film as it directly affects the nature of flake−flake junctions. Conductivity has been suggested to be maximized at either extreme: smallest flake sizes can potentially improve the quality of junctions formed between flakes, and largest flake sizes can minimize the number of junctions in a film for efficient charge transport.[22,46,47] Longer exfoliation and centrifugation time can reduce flake size by enacting more flake scission and crashing out larger flakes, while shorter times result in larger particles.[48−50] Dynamic light scattering (DLS) was used to rapidly screen the hydrodynamic particle size (Z-avg) of graphene nanosheets and directly supported these relationships

https://doi.org/10.1021/acsami.4c12664
ACS Appl. Mater. Interfaces 2024, 16, 57534−57543

across all data points in our optimization (Figure S3 of the Supporting Information). Separately, an excess of CNCs introduces an abundance of electrically insulating residue on the surface of the graphene flakes even following annealing.[25] Therefore, a balance between processing variables must be struck such that the electrical conductivity of the films is not significantly compromised in pursuit of high graphene exfoliation yield (i.e., no single globally optimal point concurrently maximizes both responses).

The Pareto frontier from our model suggests that a competitive balance is found by using high exfoliation time to produce a small flake size and accommodating for graphene exfoliation yield by using relatively low centrifugation times. The trade-off between graphene exfoliation yield and electrical conductivity can be directly determined based on CNC loading. The two end points along the Pareto frontier were found to maximize either electrical conductivity or graphene exfoliation yield with minimal compromise to the other response (points highlighted as stars in Figure 2c). In particular, electrical conductivity was maximized at conditions of 2 mg/mL of CNC loading, 600 min of exfoliation, and 30 min of centrifugation, while graphene exfoliation yield was maximized at 10 mg/mL of CNC loading, 600 min of exfoliation, and 42 min of centrifugation. These results were in stark contrast to conditions chosen from OVAT optimization; the maximized electrical conductivity condition increased electrical conductivity by 68% (3.2×10^4 S m^{-1}) and graphene exfoliation yield by 406% (3.9 mg/mL or 7.8% graphite-to-graphene conversion yield), and the maximized graphene exfoliation yield condition increased electrical conductivity by 47% (2.8×10^4 S m^{-1}) and yield by 780% (6.8 mg/mL or 13.6% graphite-to-graphene conversion yield). The multivariable optimization thus complemented empirical observations to pinpoint ideal processing conditions for graphene–CNC exfoliation. The maximum electrical conductivity conditions were used to achieve the highest performance for printable graphene–CNC inks (see below).

3.2. Characterization of Graphene Nanoplatelets. Following Bayesian optimization, optical absorbance spectroscopy and atomic force microscopy (AFM) were used to measure the concentration and dimensions of the graphene nanoplatelets, respectively. A graphene concentration of 3.92 mg/mL (7.8 wt % graphene exfoliation yield) was calculated from the optical absorbance at 660 nm via the Beer–Lambert law using a measured extinction coefficient of 3622 mL mg^{-1} m^{-1} (Figure 3a). Raman spectroscopy was also used to characterize the graphene nanoplatelets compared to the starting graphite, exhibiting an increase in the D band and a downshifted 2D band without a shoulder after exfoliation (Figure 3b). The more symmetric 2D band is indicative of the few-layer graphene structure, which generally forms a shoulder if there are five or more layers of graphene.[51,52] The increase in the D/G ratio from 0.17 to 0.35 also indicates the formation of few-layered graphene nanoplatelets with more edge defects than the starting graphite.[11] AFM showed flakes with an average lateral size of 219 ± 85 nm and thickness of 3.8 ± 1.4 nm, suggesting that few-layer nanoplatelets were successfully obtained (panels c and d of Figure 3). It should be noted that the measured thickness is larger than the theoretical height of the graphene layers since adsorbed CNC residue on the surfaces increases the measured height. Overall, the characterization of the exfoliated dispersion and films corroborate the formation of few-layer graphene nanoplatelets.

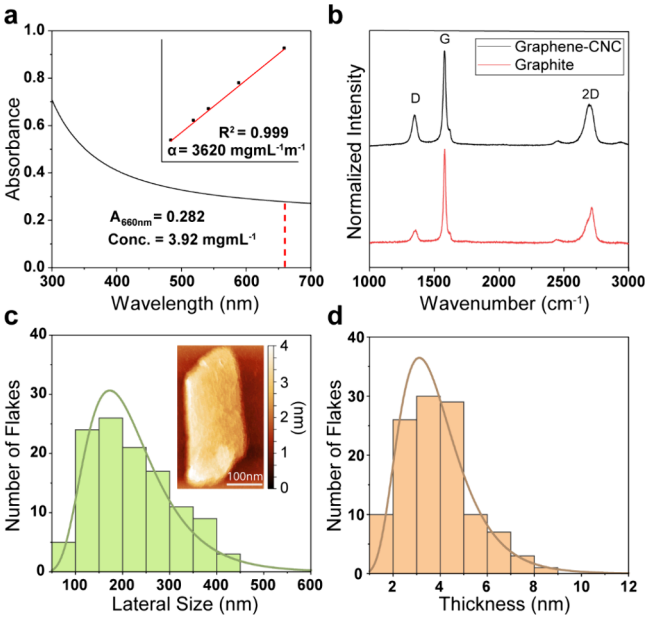

Figure 3. Characterization of graphene–CNC nanoplatelets. (a) Optical absorbance spectrum and calibration curve used for determining the graphene extinction coefficient (inset). (b) Raman spectra of raw graphite powder and exfoliated graphene–CNC nanoplatelets. (c) Histogram of atomic force microscopy (AFM) measurements for graphene flake (n = 116 flakes) lateral size (measured as square root of mean flake area) and representative AFM image of an individual graphene–CNC nanoplatelet (inset). (d) Histogram of AFM measurements for graphene flake thickness (n = 116 flakes). A log-normal curve was fit to the AFM histogram data.

3.3. Formulation of Aerosol Jet Printing Ink. Aerosol jet printing (AJP) was used to pattern the high-concentration graphene–CNC dispersion. The exfoliated dispersion was used directly after centrifugation without any additional processing steps, which significantly improves ease of use compared to other reports that require solvent exchange or concentration via evaporation. However, despite achieving a printable film, directly inputting the graphene–CNC dispersion into AJP leads to suboptimal line resolution issues due to overspray and inconsistent spreading (Figure 4c). Hence, additives were considered to alter the viscosity and volatility of the AJP ink to reproducibly print high-resolution features.

Common additives for graphene ink formulation include ethylene glycol, terpineol, or other nonvolatile and viscous solvents that can adjust rheological properties to suit different printing needs.[17,53,54] While some of these solvents have the potential to be sustainably sourced, they generally carry concerns related to toxicity, biocompatibility, and safety. Recently, it was found that graphene disperses well in cyrene, a biorenewable cellulose-based solvent that has high viscosity and low volatility.[10,28,55] By increasing the concentration of cyrene added to the graphene–CNC dispersion, we were able to tune the viscosity of ink from 1 to 14 mPa s^{-1}, indicating that we can directly formulate the graphene–CNC ink to fulfill requirements of different printing techniques (Figure 4a). The final ink formulation for AJP only required 5% (v/v) cyrene to marginally increase the viscosity of the ink, and 30% (v/v) ethanol to decrease the boiling point for more efficient drying. The viscosity of the final graphene–CNC ink was 1.5 mPa s^{-1}, which falls within the specifications for AJP (Figure 4d).[56] Based on optical microscopy images, uniform and high-

https://doi.org/10.1021/acsami.4c12664
ACS Appl. Mater. Interfaces 2024, 16, 57534–57543

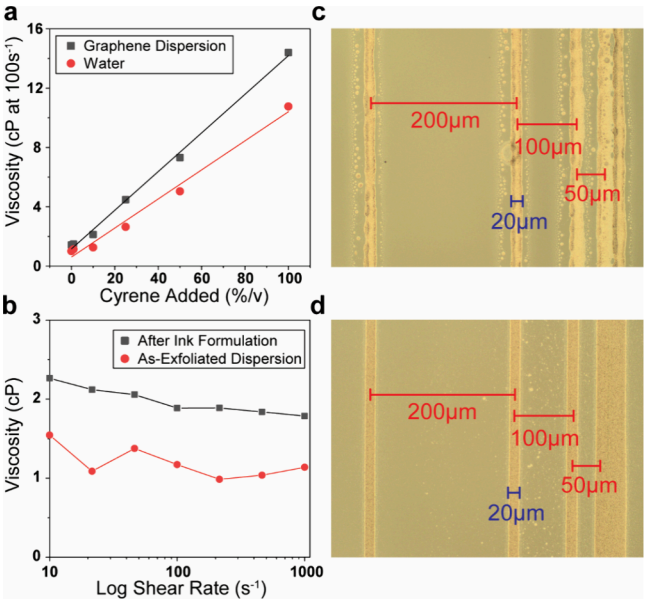

Figure 4. Printing resolution and optimization of graphene−CNC during aerosol jet printing (AJP). (a) Adjustment of AJP ink viscosity based on cyrene content demonstrates the tunability of graphene aqueous dispersions over the range of 1−14 cP (R^2 > 0.99 for both curves). (b) Viscosity curves for the final graphene−CNC ink formulation and as-exfoliated graphene dispersion. (c) Optical micrograph of AJP graphene lines produced from the as-exfoliated graphene dispersion. (d) Optical micrograph of AJP graphene lines after ink formulation optimization.

resolution lines were achieved with ∼20 μm line width and 50 μm line spacing (Figure 4b), which enables the patterning of detailed components such as interdigitated electrodes.[57] Furthermore, the formulated ink remained stable after 6 months and showed highly negative zeta potential from DLS for both the diluted raw dispersion (−47.7 mV) and formulated ink (−44.8 mV) (Figure S5 of the Supporting Information). Thus, this graphene ink formulation with only cellulose-derived additives was deemed to be a stable colloidal dispersion with shelf life appropriate for commercial printing applications.

3.4. Performance of Aerosol Jet Printed Graphene Films. The optimized ink formulation was then used to print thin films on glass slides and polyimide substrates (Figure 5a). AJP allowed for precise printing of multiple layers to achieve a thicker film with lower sheet resistance (Figure 5b). A 3-layer printed film on glass achieved a high electrical conductivity of $2.2 \pm 0.1 \times 10^4$ S m^{-1} after annealing at 350 °C in air. This electrical conductivity is competitive with other reports of aqueous-based graphene printing, and the highest for AJP without the use of harmful additives or dopants.[20,58−60] This high electrical conductivity can be attributed to the decomposition of the CNCs that leaves behind an sp^2-rich residue on the surface of the graphene similar to previous observations for graphene inks with ethyl cellulose.[17,61] This carbonaceous char provides improved charge transport by bridging flake−flake junctions to create a more continuous percolating film. Indeed, a uniform and dense percolating network of graphene nanoplatelets was observed in scanning electron micrographs of the film surface (Figure 5b). Cross-

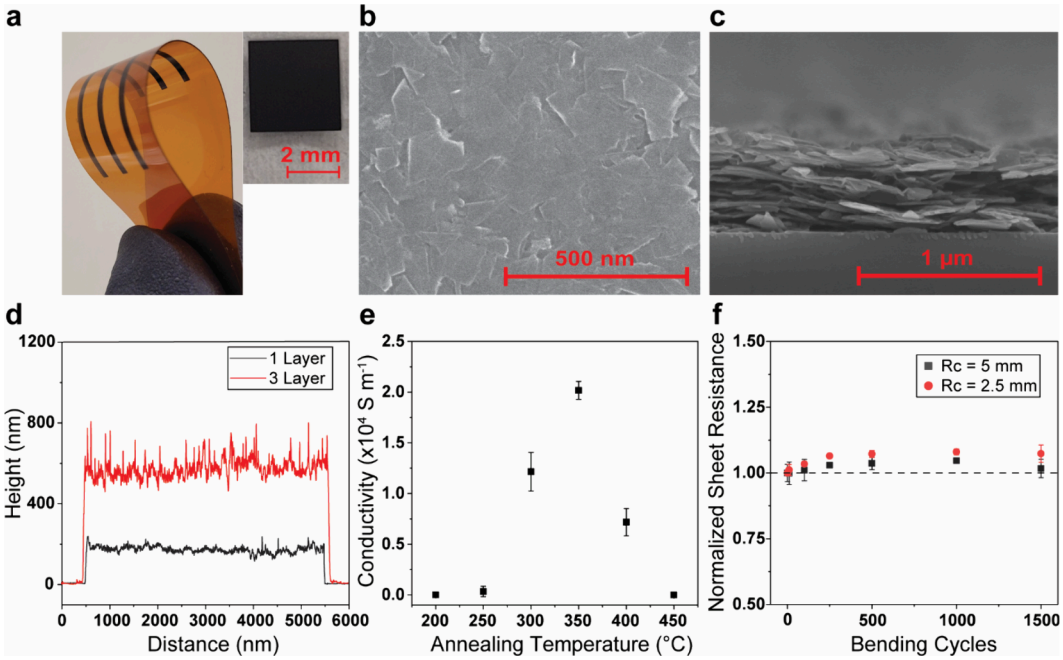

Figure 5. Performance of graphene−CNC AJP films. (a) Photographs of graphene−CNC 3-layer AJP films on polyimide and glass. (b) Scanning electron micrograph of the graphene−CNC film surface. (c) Scanning electron micrograph of a cross-section of the graphene−CNC 3-layer film. (d) Profilometry scans of the surfaces of 1- and 3-layer graphene−CNC films, which allow the height of the final printed films to be extracted. (e) Electrical conductivity of graphene−CNC 3-layer films as a function of the post-printing annealing temperature, suggesting effective CNC decomposition beyond 250 °C and compromised conductivity due to graphene oxidation above 350 °C. Triplicate measurements of both conductivity and thickness of films were taken to confirm this behavior, with associated error bars generated from the propagated standard deviation. (f) Normalized sheet resistance of the graphene−CNC 3-layer film when folded to a radius of curvature of 2.5 and 5 mm, showing retention of conductivity over 1500 bending cycles. The sheet resistance is normalized to the value prior to bending. High reproducibility is demonstrated by the small error bars that were generated from the propagated standard deviation from triplicate measurements of sheet resistance.

https://doi.org/10.1021/acsami.4c12664
ACS Appl. Mater. Interfaces 2024, 16, 57534−57543

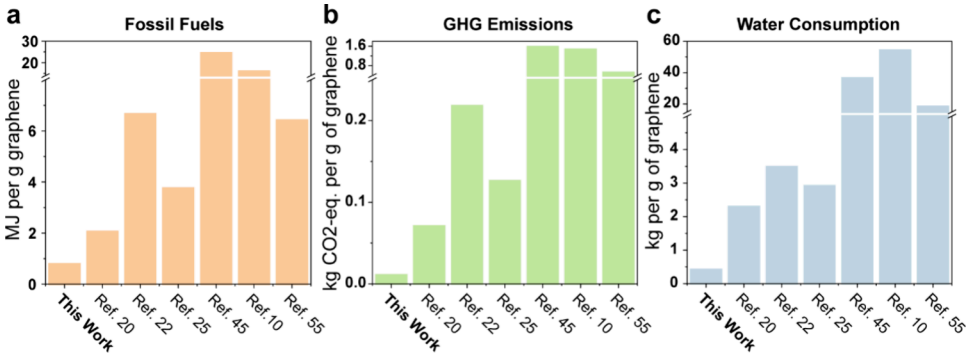

Figure 6. Life cycle assessment. Raw materials life cycle assessment comparison for recently published electronic-grade graphene inks that were nominally produced using eco-friendly liquid-phase exfoliation: (a) Fossil fuel energy required, (b) greenhouse gas emissions, and (c) water consumption. In all cases, the reported numbers are per gram of graphene produced.

sectional images of multiple-layer printed films also showed well-aligned stacking of graphene flakes (Figure 5c). The dependence of the film electrical conductivity on the post-printing annealing temperature demonstrates the importance of the sp^2-rich residue formation, where the greatest conductivity was measured at 350 °C (Figure 5e). Thermogravimetric analysis (TGA) suggests that the majority of the weight loss from CNCs occurs for temperatures between 200 and 300 °C (Figure S2e of the Supporting Information). The mechanical resilience of the graphene−CNC films was also tested by measuring the electrical conductivity of the film over many bending cycles (Figure 5f). Even after 1500 bending cycles at a radius of 1.5 mm, minimal changes in the film electrical conductivity were observed, thus confirming the suitability of printed graphene−CNC films for flexible electronic applications.

3.5. Life Cycle Assessment. To assess the sustainability and environmental friendliness of the graphene−CNC ink, we performed raw material life cycle assessment (LCA) in comparison to other electronic-grade graphene inks that were nominally produced using eco-friendly liquid-phase exfoliation. In each comparison case, electronic-grade was defined as achieving a film electrical conductivity exceeding 10^4 S m^{-1} (Figure 6). The comparative LCA indicates that the raw materials used in the graphene−CNC ink have the lowest fossil energy usage, GHG emissions, and water consumption by margins of 62, 84, and 63%, respectively compared to the next best performing ink.[20] These improvements can be attributed in part to the high yield of graphene produced using CNCs, where the graphite used per gram of graphene produced is notably low compared to other LPE-derived inks. In addition, the use of aqueous media and biorenewable, cellulose-based additives provides further environmental benefits. If we expand the LCA system boundary to include the electricity consumed in exfoliation, purification, or other processing instruments in our bench-scale process, we estimate that this would add 41 MJ of fossil fuels, 3.0 kg of CO_2 equiv of GHG emissions, and 25 kg of water consumption (Table S3 of the Supporting Information). However, at industrial scale, sonication would be replaced by large-scale shear mixing or wet jet milling, where the electricity costs per unit gram of graphene produced would be reduced by greater than an order of magnitude and ultimately be comparable to or less than the electricity demands of competing electronic-grade graphene inks. Therefore, our comparative LCA illustrates that the utilization of CNCs as a graphene dispersant has significant eco-friendliness advantages compared to incumbent procedures.

3.6. Molecular Dynamics Simulations. Since previous work using CNCs to exfoliate graphene has employed CNCs functionalized with sulfate half ester surface groups,[25,33] we conducted molecular dynamics simulations on our carboxylated CNCs to confirm that they also aid graphene exfoliation via their amphiphilicity. In particular, molecular dynamics simulations were performed on CNC−COO^-Na^+ to determine binding energies based on the potential of mean force (PMF) calculations. The PMF profile resulting from pushing the (100) surface of CNC−COO^- to the graphene surface is displayed in Figure S6a of the Supporting Information, where the PMF difference between the separated (d = 2.82 nm) and aggregated (PMF minimum at d = 1.36 nm) states indicates a negative free energy of −66 kcal mol^{-1}, which suggests a high binding affinity of the CNC−COO^- (100) hydrophobic surface to graphene. Meanwhile, simulations of the CNC−COO^- (110) hydrophilic surface binding to graphene resulted in unstable contact, where the CNC−COO^- lattice rotated around the chain length axis to the more favorable (100) adsorption to graphene. These observations agree with previous reports using analogous models, such that only the hydrophobic face of the CNCs binds favorably to graphene.[62,63]

Next, we confirmed that the (110) surfaces of CNC−COO^- with negatively charged carboxyl groups would repel each other to assist with exfoliation of graphite. Indeed, the approach of a free-CNC−COO^- (110) to the fixed (110) face led to excessive force build-up (after 16 ns) that breaks the crystallinity of the free-CNC−COO^- (Figure S7a of the Supporting Information), all without direct contact between the two CNC−COO^- (110) surfaces. This result implies that the repulsion between the charged surfaces impedes aggregation, and any added external force only disrupts the crystallinity of the CNC−COO^-. To further examine the influence of repulsive interactions on the binding free energies, we carried out PMF calculations on the reaction coordinate generated by pulling apart two initially contacting crystals. Pristine CNC (CNC with only surface −OH groups) and CNC−COO^- were compared to observe the effect of the charged surface groups. As displayed in Figure S7b of the Supporting Information, the absolute value of the binding free energy is significantly reduced from 96 kcal mol^{-1} to 24 kcal mol^{-1} with carboxylated CNCs, caused by the added repulsive interaction of the functionalized surface. Moreover, the pristine

https://doi.org/10.1021/acsami.4c12664
ACS Appl. Mater. Interfaces 2024, 16, 57534−57543

CNC travels a barrier-free path to bind, while CNC−COO^- confronts a 4.5 kcal mol^{-1} energy barrier at the 2.55 nm point on the reaction coordinate, which prevents the binding of the CNC−COO^-. These observations corroborate earlier work, which showed that the charge density increment of the carboxylate groups elevates the repulsive inter-CNC−COO^- interactions to prevent binding.[64] In summary, our PMF calculations revealed that carboxylated CNCs (100) surfaces have a high tendency to bind to graphene and that the outward facing (110) surfaces impede aggregation with electrostatic repulsion to enhance graphene exfoliation and colloidal stability.

4. CONCLUSION

In this work, we have developed an environmentally friendly pathway to exfoliating graphene nanosheets by harnessing biorenewable MxG-derived CNCs. Three variables from the exfoliation procedure were optimized simultaneously using a Bayesian machine learning model, allowing the identification of conditions that produce concurrently high graphene exfoliation yield and electrical conductivity of vacuum-filtered films. The optimized graphene−CNC dispersion was directly formulated to an AJP ink using cellulose-based additives of cyrene and ethanol, resulting in films with conductivity comparable to other electronic-grade aqueous graphene inks. High-resolution printing of films with superlative mechanical resilience suggests that the bioderived graphene−CNC ink can be employed for intricate device designs in flexible electronics. Furthermore, LCA of our graphene−CNC exfoliation process compared to other environmentally friendly approaches indicates that the raw materials in our electronic-grade ink have the lowest fossil fuel consumption, greenhouse gas emissions, and water consumption. In addition to the use of biorenewable raw materials, this eco-friendliness can be attributed to the exceptionally high graphene exfoliation yield of carboxylated CNCs, which is consistent with molecular dynamics calculations of the favorable binding of the CNC (100) hydrophobic faces to graphene and the repulsive interactions between the CNC (110) hydrophilic faces. Overall, this work establishes biorenewable carboxylated CNCs as the key enabler for efficient, scalable, eco-friendly, and sustainable manufacturing of electronic-grade graphene inks for printable and flexible electronics.

■ ASSOCIATED CONTENT

Supporting Information

The Supporting Information is available free of charge at https://pubs.acs.org/doi/10.1021/acsami.4c12664.

Additional characterization methodology, detailed characterization of the synthesized biorenewable CNCs, one-variable-at-a-time optimization results, dynamic light scattering measurements, additional graphene flake characterization, and molecular dynamics simulation results (PDF)

■ AUTHOR INFORMATION

Corresponding Author

Mark C. Hersam − *Department of Materials Science and Engineering, Northwestern University, Evanston, Illinois 60208, United States; Department of Chemistry, Northwestern University, Evanston, Illinois 60208, United States; Department of Electrical and Computer Engineering, Northwestern University, Evanston, Illinois 60208, United States;* orcid.org/0000-0003-4120-1426; Email: m-hersam@northwestern.edu

Authors

Janan Hui − *Department of Chemistry, Northwestern University, Evanston, Illinois 60208, United States*

Haoyang You − *Department of Chemistry, University of Chicago, Chicago, Illinois 60637, United States;* orcid.org/0000-0001-7462-2118

Anton Van Beek − *Department of Mechanical Engineering, Northwestern University, Evanston, Illinois 60208, United States*

Jinrui Zhang − *Department of Chemical and Biological Engineering, Northwestern University, Evanston, Illinois 60208, United States;* orcid.org/0000-0002-9468-070X

Arash Elahi − *Department of Chemical Engineering, University of Illinois at Chicago, Chicago, Illinois 60607, United States;* orcid.org/0000-0003-1687-3781

Julia R. Downing − *Department of Materials Science and Engineering, Northwestern University, Evanston, Illinois 60208, United States*

Lindsay E. Chaney − *Department of Materials Science and Engineering, Northwestern University, Evanston, Illinois 60208, United States*

DoKyoung Lee − *Department of Crop Sciences, University of Illinois at Urbana−Champaign, Urbana, Illinois 61801, United States*

Elizabeth A. Ainsworth − *Global Change and Photosynthesis Research Unit, Agricultural Research Service (ARS), United States Department of Agriculture (USDA), Urbana, Illinois 61801, United States*

Santanu Chaudhuri − *Department of Chemical Engineering, University of Illinois at Chicago, Chicago, Illinois 60607, United States; Department of Civil, Materials, and Environmental Engineering, University of Illinois at Chicago, Chicago, Illinois 60607, United States;* orcid.org/0000-0002-4328-2947

Jennifer B. Dunn − *Department of Chemical and Biological Engineering, Northwestern University, Evanston, Illinois 60208, United States;* orcid.org/0000-0002-2065-5106

Wei Chen − *Department of Mechanical Engineering, Northwestern University, Evanston, Illinois 60208, United States;* orcid.org/0000-0002-4653-7124

Stuart J. Rowan − *Department of Chemistry, University of Chicago, Chicago, Illinois 60637, United States; Pritzker School of Molecular Engineering, University of Chicago, Chicago, Illinois 60637, United States; Chemical and Engineering Sciences, Argonne National Laboratory, Lemont, Illinois 60439, United States;* orcid.org/0000-0001-8176-0594

Complete contact information is available at: https://pubs.acs.org/10.1021/acsami.4c12664

Author Contributions

†Janan Hui and Haoyang You contributed equally to this work.

Notes

The authors declare no competing financial interest.

■ ACKNOWLEDGMENTS

This work was primarily supported by the National Science Foundation MADE-PUBLIC Future Manufacturing Research

Grant Program (NSF Award CMMI-2037026). Additional support for the aerosol jet printing was provided by the U.S. Department of Commerce, National Institute of Standards and Technology (Award 70NANB19H005) as part of the Center for Hierarchical Materials Design (CHiMaD). This work made use of the EPIC and Keck-II facilities within the Northwestern University NUANCE Center, which has received support from the SHyNE Resource (NSF ECCS-2025633) and the Northwestern University Materials Research Science and Engineering Center (MRSEC) (NSF DMR-2308691). This work also made use of the MatCI facility at Northwestern University, which is supported by the Northwestern University MRSEC (NSF DMR-2308691).

■ ABBREVIATIONS USED

CNC, cellulose nanocrystal; MxG, *Miscanthus* × *giganteus*; LPE, liquid-phase exfoliation; EC, ethyl cellulose; GHG, greenhouse gas; LCA, life cycle assessment; PMF, potential of mean force; MD, molecular dynamics; OVAT, one variable at a time; AFM, atomic force microscopy; DLS, dynamic light scattering; AJP, aerosol jet printing

■ REFERENCES

(1) Tiwari, S. K.; Sahoo, S.; Wang, N.; Huczko, A. Graphene Research and Their Outputs: Status and Prospect. *J. Sci. Adv. Mater. Devices* **2020**, *5* (1), 10−29.
(2) Soldano, C.; Mahmood, A.; Dujardin, E. Production, Properties and Potential of Graphene. *Carbon* **2010**, *48* (8), 2127−2150.
(3) El-Kady, M. F.; Shao, Y.; Kaner, R. B. Graphene for Batteries, Supercapacitors and Beyond. *Nat. Rev. Mater.* **2016**, *1* (7), 16033.
(4) Olabi, A. G.; Abdelkareem, M. A.; Wilberforce, T.; Sayed, E. T. Application of Graphene in Energy Storage Device - A Review. *Renewable Sustainable Energy Rev.* **2021**, *135*, 110026.
(5) Kong, M.; Yang, M.; Li, R.; Long, Y.-Z.; Zhang, J.; Huang, X.; Cui, X.; Zhang, Y.; Said, Z.; Li, C. Graphene-Based Flexible Wearable Sensors: Mechanisms, Challenges, and Future Directions. *Int. J. Adv. Manuf. Technol.* **2024**, *131* (5−6), 3205−3237.
(6) Zhang, H.; He, R.; Niu, Y.; Han, F.; Li, J.; Zhang, X.; Xu, F. Graphene-Enabled Wearable Sensors for Healthcare Monitoring. *Biosens. Bioelectron.* **2022**, *197*, 113777.
(7) Miao, J.; Fan, T. Flexible and Stretchable Transparent Conductive Graphene-Based Electrodes for Emerging Wearable Electronics. *Carbon* **2023**, *202*, 495−527.
(8) Lin, L.; Peng, H.; Liu, Z. Synthesis Challenges for Graphene Industry. *Nat. Mater.* **2019**, *18* (6), 520−524.
(9) Safian, M. T.; Umar, K.; Mohamad Ibrahim, M. N. Synthesis and Scalability of Graphene and Its Derivatives: A Journey towards Sustainable and Commercial Material. *J. Clean. Prod.* **2021**, *318*, 128603.
(10) Pan, K.; Fan, Y.; Leng, T.; Li, J.; Xin, Z.; Zhang, J.; Hao, L.; Gallop, J.; Novoselov, K. S.; Hu, Z. Sustainable Production of Highly Conductive Multilayer Graphene Ink for Wireless Connectivity and IoT Applications. *Nat. Commun.* **2018**, *9* (1), 5197.
(11) Paton, K. R.; Varrla, E.; Backes, C.; Smith, R. J.; Khan, U.; O'Neill, A.; Boland, C.; Lotya, M.; Istrate, O. M.; King, P.; Higgins, T.; Barwich, S.; May, P.; Puczkarski, P.; Ahmed, I.; Moebius, M.; Pettersson, H.; Long, E.; Coelho, J.; O'Brien, S. E.; McGuire, E. K.; Sanchez, B. M.; Duesberg, G. S.; McEvoy, N.; Pennycook, T. J.; Downing, C.; Crossley, A.; Nicolosi, V.; Coleman, J. N. Scalable Production of Large Quantities of Defect-Free Few-Layer Graphene by Shear Exfoliation in Liquids. *Nat. Mater.* **2014**, *13* (6), 624−630.
(12) Xu, Y.; Cao, H.; Xue, Y.; Li, B.; Cai, W. Liquid-Phase Exfoliation of Graphene: An Overview on Exfoliation Media, Techniques, and Challenges. *Nanomaterials* **2018**, *8* (11), 942.
(13) Salavagione, H. J.; Sherwood, J.; De bruyn, M.; Budarin, V. L.; Ellis, G. J.; Clark, J. H.; Shuttleworth, P. S. Identification of High Performance Solvents for the Sustainable Processing of Graphene. *Green Chem.* **2017**, *19* (11), 2550−2560.
(14) Zhang, H.; Wu, Y.; Yang, F.; Dong, H.; Bian, Y.; Jia, H.; Xie, X.; Zhang, J. Using Cellulose Nanocrystal as Adjuvant to Improve the Dispersion Ability of Multilayer Graphene in Aqueous Suspension. *Front. Bioeng. Biotechnol.* **2021**, *9*, 638744.
(15) Han, X.; Gao, J.; Chen, T.; Zhao, Y. Interfacial Interaction and Steric Repulsion in Polymer-Assisted Liquid Exfoliation to Produce High-Quality Graphene. *Chem. Pap.* **2020**, *74* (3), 757−765.
(16) Parviz, D.; Das, S.; Ahmed, H. S. T.; Irin, F.; Bhattacharia, S.; Green, M. J. Dispersions of Non-Covalently Functionalized Graphene with Minimal Stabilizer. *ACS Nano* **2012**, *6* (10), 8857−8867.
(17) Secor, E. B.; Prabhumirashi, P. L.; Puntambekar, K.; Geier, M. L.; Hersam, M. C. Inkjet Printing of High Conductivity, Flexible Graphene Patterns. *J. Phys. Chem. Lett.* **2013**, *4* (8), 1347−1351.
(18) Lotya, M.; King, P. J.; Khan, U.; De, S.; Coleman, J. N. High-Concentration, Surfactant-Stabilized Graphene Dispersions. *ACS Nano* **2010**, *4* (6), 3155−3162.
(19) Lund, S.; Kauppila, J.; Sirkiä, S.; Palosaari, J.; Eklund, O.; Latonen, R.-M.; Smått, J.-H.; Peltonen, J.; Lindfors, T. Fast High-Shear Exfoliation of Natural Flake Graphite with Temperature Control and High Yield. *Carbon* **2021**, *174*, 123−131.
(20) Carey, T.; Alhourani, A.; Tian, R.; Seyedin, S.; Arbab, A.; Maughan, J.; Šiller, L.; Horvath, D.; Kelly, A.; Kaur, H.; Caffrey, E.; Kim, J. M.; Hagland, H. R.; Coleman, J. N. Cyclic Production of Biocompatible Few-Layer Graphene Ink with in-Line Shear-Mixing for Inkjet-Printed Electrodes and Li-Ion Energy Storage. *Npj 2D Mater. Appl.* **2022**, *6* (1), 3.
(21) Girish, S.; Tambe, P. Surfactant Assisted Exfoliation of High Purity Graphene in Aqueous Solution as a Nanofluid Using Kitchen Blender: Influence on Dispersion, Thermal Conductivity and Rheological Properties. *Adv. Powder Technol.* **2022**, *33* (10), 103767.
(22) Large, M. J.; Ogilvie, S. P.; Amorim Graf, A.; Lynch, P. J.; O'Mara, M. A.; Waters, T.; Jurewicz, I.; Salvage, J. P.; Dalton, A. B. Large-Scale Surfactant Exfoliation of Graphene and Conductivity-Optimized Graphite Enabling Wireless Connectivity. *Adv. Mater. Technol.* **2020**, *5* (7), 2000284.
(23) Hyun, W. J.; Secor, E. B.; Hersam, M. C. White Paper: Printable Graphene Inks Stabilized with Cellulosic Polymers. *MRS Bull.* **2018**, *43* (10), 730−733.
(24) Kemal, S. I.; Uribe Ortiz, C. A.; Sharma, V. Surface Forces and Stratification in Foam Films Formed with Bile Salts. *Mol. Syst. Des. Eng.* **2021**, *6* (7), 520−533.
(25) Lund, S.; Björnvik, E.; Wang, Q.; Wang, X.; Vajravel, S.; Wey, L. T.; Allahverdiyeva, Y.; Kauppila, J.; Smått, J.-H.; Peltonen, J.; Latonen, R.-M.; Lindfors, T. Shear Exfoliated Few-Layer Graphene and Cellulose Nanocrystal Composite as Biocompatible Anode with Efficient Charge Transfer. *Carbon Trends* **2022**, *9*, 100210.
(26) Narayan, R.; Kim, S. O. Surfactant Mediated Liquid Phase Exfoliation of Graphene. *Nano Converg.* **2015**, *2* (1), 20.
(27) Salavagione, H. J.; Sherwood, J.; De bruyn, M.; Budarin, V. L.; Ellis, G. J.; Clark, J. H.; Shuttleworth, P. S. Identification of High Performance Solvents for the Sustainable Processing of Graphene. *Green Chem.* **2017**, *19* (11), 2550−2560.
(28) Fernandes, J.; Nemala, S. S.; De Bellis, G.; Capasso, A. Green Solvents for the Liquid Phase Exfoliation Production of Graphene: The Promising Case of Cyrene. *Front. Chem.* **2022**, *10*, 878799.
(29) Morton, J. A.; Kaur, A.; Khavari, M.; Tyurnina, A. V.; Priyadarshi, A.; Eskin, D. G.; Mi, J.; Porfyrakis, K.; Prentice, P.; Tzanakis, I. An Eco-Friendly Solution for Liquid Phase Exfoliation of Graphite under Optimised Ultrasonication Conditions. *Carbon* **2023**, *204*, 434−446.
(30) Ng, K. L.; Maciejewska, B. M.; Qin, L.; Johnston, C.; Barrio, J.; Titirici, M.-M.; Tzanakis, I.; Eskin, D. G.; Porfyrakis, K.; Mi, J.; Grobert, N. Direct Evidence of the Exfoliation Efficiency and Graphene Dispersibility of Green Solvents toward Sustainable Graphene Production. *ACS Sustainable Chem. Eng.* **2023**, *11* (1), 58−66.

https://doi.org/10.1021/acsami.4c12664
ACS Appl. Mater. Interfaces 2024, 16, 57534−57543

(31) George, J.; S N, S. Cellulose Nanocrystals: Synthesis, Functional Properties, and Applications. *Nanotechnol. Sci. Appl.* **2015**, 45.
(32) Trache, D.; Thakur, V. K.; Boukherroub, R. Cellulose Nanocrystals/Graphene Hybrids—A Promising New Class of Materials for Advanced Applications. *Nanomaterials* **2020**, *10* (8), 1523.
(33) Carrasco, P. M.; Montes, S.; García, I.; Borghei, M.; Jiang, H.; Odriozola, I.; Cabañero, G.; Ruiz, V. High-Concentration Aqueous Dispersions of Graphene Produced by Exfoliation of Graphite Using Cellulose Nanocrystals. *Carbon* **2014**, *70*, 157−163.
(34) Cao, J.; Zhang, X.; Wu, X.; Wang, S.; Lu, C. Cellulose Nanocrystals Mediated Assembly of Graphene in Rubber Composites for Chemical Sensing Applications. *Carbohydr. Polym.* **2016**, *140*, 88−95.
(35) Liu, K.; Hu, J.; Kong, Z.; Hu, J.; Tian, Z.; Hou, J.; Qin, J.; Liu, C.; Liang, S.; Wu, H.; Zhang, J.; Zong, L.; Duan, Y. High-Yield, High-Conductive Graphene/Nanocellulose Hybrids Prepared by Co-Exfoliation of Low-Oxidized Expanded Graphite and Microfibrillated Cellulose. *Compos. Part B Eng.* **2021**, *225*, 109250.
(36) Oehme, D. P.; Downton, M. T.; Doblin, M. S.; Wagner, J.; Gidley, M. J.; Bacic, A. Unique Aspects of the Structure and Dynamics of Elementary I β Cellulose Microfibrils Revealed by Computational Simulations. *Plant Physiol.* **2015**, *168* (1), 3−17.
(37) Nishiyama, Y.; Langan, P.; Chanzy, H. Crystal Structure and Hydrogen-Bonding System in Cellulose Iβ from Synchrotron X-Ray and Neutron Fiber Diffraction. *J. Am. Chem. Soc.* **2002**, *124* (31), 9074−9082.
(38) Ding, S.-Y.; Zhao, S.; Zeng, Y. Size, Shape, and Arrangement of Native Cellulose Fibrils in Maize Cell Walls. *Cellulose* **2014**, *21* (2), 863−871.
(39) Cudjoe, E.; Hunsen, M.; Xue, Z.; Way, A. E.; Barrios, E.; Olson, R. A.; Hore, M. J. A.; Rowan, S. J. Miscanthus Giganteus: A Commercially Viable Sustainable Source of Cellulose Nanocrystals. *Carbohydr. Polym.* **2017**, *155*, 230−241.
(40) International Organization for Standardization (ISO). *ISO 14040:2006 Environmental Management—Life Cycle Assessment—Principles and Framework*; ISO: Geneva, Switzerland, 2006; https://www.iso.org/standard/37456.html.
(41) International Organization for Standardization (ISO). *ISO 14044:2006 Environmental Management—Life Cycle Assessment—Requirements and Guidelines*; ISO: Geneva, Switzerland, 2006; https://www.iso.org/standard/38498.html.
(42) Kumar, S.; Rosenberg, J. M.; Bouzida, D.; Swendsen, R. H.; Kollman, P. A. THE Weighted Histogram Analysis Method for Free-Energy Calculations on Biomolecules. I. The Method. *J. Comput. Chem.* **1992**, *13* (8), 1011−1021.
(43) Cai, X.; Jiang, Z.; Zhang, X.; Zhang, X. Effects of Tip Sonication Parameters on Liquid Phase Exfoliation of Graphite into Graphene Nanoplatelets. *Nanoscale Res. Lett.* **2018**, *13* (1), 241.
(44) Vacacela Gomez, C.; Guevara, M.; Tene, T.; Villamagua, L.; Usca, G. T.; Maldonado, F.; Tapia, C.; Cataldo, A.; Bellucci, S.; Caputi, L. S. The Liquid Exfoliation of Graphene in Polar Solvents. *Appl. Surf. Sci.* **2021**, *546*, 149046.
(45) Chaney, L. E.; Van Beek, A.; Downing, J. R.; Zhang, J.; Zhang, H.; Hui, J.; Sorensen, E. A.; Khalaj, M.; Dunn, J. B.; Chen, W.; Hersam, M. C. Bayesian Optimization of Environmentally Sustainable Graphene Inks Produced by Wet Jet Milling. *Small* **2024**, *20*, 2309579.
(46) Kelly, A. G.; O'Suilleabhain, D.; Gabbett, C.; Coleman, J. N. The Electrical Conductivity of Solution-Processed Nanosheet Networks. *Nat. Rev. Mater.* **2022**, *7*, 217.
(47) Rizzi, L.; Wijaya, A. F.; Palanisamy, L. V.; Schuster, J.; Köhne, M.; Schulz, S. E. Quantifying the Influence of Graphene Film Nanostructure on the Macroscopic Electrical Conductivity. *Nano Express* **2020**, *1* (2), 020035.
(48) Khan, U.; O'Neill, A.; Porwal, H.; May, P.; Nawaz, K.; Coleman, J. N. Size Selection of Dispersed, Exfoliated Graphene Flakes by Controlled Centrifugation. *Carbon* **2012**, *50* (2), 470−475.
(49) Khan, U.; O'Neill, A.; Lotya, M.; De, S.; Coleman, J. N. High-Concentration Solvent Exfoliation of Graphene. *Small* **2010**, *6* (7), 864−871.
(50) Li, Z.; Young, R. J.; Backes, C.; Zhao, W.; Zhang, X.; Zhukov, A. A.; Tillotson, E.; Conlan, A. P.; Ding, F.; Haigh, S. J.; Novoselov, K. S.; Coleman, J. N. Mechanisms of Liquid-Phase Exfoliation for the Production of Graphene. *ACS Nano* **2020**, *14* (9), 10976−10985.
(51) Ferrari, A. C.; Meyer, J. C.; Scardaci, V.; Casiraghi, C.; Lazzeri, M.; Mauri, F.; Piscanec, S.; Jiang, D.; Novoselov, K. S.; Roth, S.; Geim, A. K. Raman Spectrum of Graphene and Graphene Layers. *Phys. Rev. Lett.* **2006**, *97* (18), 187401.
(52) Ferrari, A. C. Raman Spectroscopy of Graphene and Graphite: Disorder, Electron-Phonon Coupling, Doping and Nonadiabatic Effects. *Solid State Commun.* **2007**, *143* (1−2), 47−57.
(53) Gamba, L.; Johnson, Z. T.; Atterberg, J.; Diaz-Arauzo, S.; Downing, J. R.; Claussen, J. C.; Hersam, M. C.; Secor, E. B. Systematic Design of a Graphene Ink Formulation for Aerosol Jet Printing. *ACS Appl. Mater. Interfaces* **2023**, *15* (2), 3325−3335.
(54) Romagnoli, M.; Lassinantti Gualtieri, M.; Cannio, M.; Barbieri, F.; Giovanardi, R. Preparation of an Aqueous Graphitic Ink for Thermal Drop-on-Demand Inkjet Printing. *Mater. Chem. Phys.* **2016**, *182*, 263−271.
(55) Tkachev, S.; Monteiro, M.; Santos, J.; Placidi, E.; Hassine, M. B.; Marques, P.; Ferreira, P.; Alpuim, P.; Capasso, A. Environmentally Friendly Graphene Inks for Touch Screen Sensors. *Adv. Funct. Mater.* **2021**, *31* (33), 2103287.
(56) Jabari, E.; Toyserkani, E. Micro-Scale Aerosol-Jet Printing of Graphene Interconnects. *Carbon* **2015**, *91*, 321−329.
(57) Parate, K.; Rangnekar, S. V.; Jing, D.; Mendivelso-Perez, D. L.; Ding, S.; Secor, E. B.; Smith, E. A.; Hostetter, J. M.; Hersam, M. C.; Claussen, J. C. Aerosol-Jet-Printed Graphene Immunosensor for Label-Free Cytokine Monitoring in Serum. *ACS Appl. Mater. Interfaces* **2020**, *12* (7), 8592−8603.
(58) Kaindl, R.; Gupta, T.; Blümel, A.; Pei, S.; Hou, P.-X.; Du, J.; Liu, C.; Patter, P.; Popovic, K.; Dergez, D.; Elibol, K.; Schafler, E.; Liu, J.; Eder, D.; Kieslinger, D.; Ren, W.; Hartmann, P.; Waldhauser, W.; Bayer, B. C. Aerosol Jet Printing of Graphene and Carbon Nanotube Patterns on Realistically Rugged Substrates. *ACS Omega* **2021**, *6* (50), 34301−34313.
(59) Al Shboul, A.; Ketabi, M.; Izquierdo, R. Conductive Green Graphene Inks for Printed Electronics. *Proceedings of the 2021 IEEE 16th Nanotechnology Materials and Devices Conference (NMDC)*; Vancouver, British Columbia, Canada, Dec 12−15, 2021; pp 1−4, DOI: 10.1109/NMDC50713.2021.9677537.
(60) Majee, S.; Liu, C.; Wu, B.; Zhang, S.-L.; Zhang, Z.-B. Ink-Jet Printed Highly Conductive Pristine Graphene Patterns Achieved with Water-Based Ink and Aqueous Doping Processing. *Carbon* **2017**, *114*, 77−83.
(61) de Moraes, A. C. M.; Obrzut, J.; Sangwan, V. K.; Downing, J. R.; Chaney, L. E.; Patel, D. K.; Elmquist, R. E.; Hersam, M. C. Elucidating Charge Transport Mechanisms in Cellulose-Stabilized Graphene Inks. *J. Mater. Chem. C* **2020**, *8* (43), 15086−15091.
(62) Mianehrow, H.; Berglund, L. A.; Wohlert, J. Interface Effects from Moisture in Nanocomposites of 2D Graphene Oxide in Cellulose Nanofiber (CNF) Matrix - A Molecular Dynamics Study. *J. Mater. Chem. A* **2022**, *10* (4), 2122−2132.
(63) Alqus, R.; Eichhorn, S. J.; Bryce, R. A. Molecular Dynamics of Cellulose Amphiphilicity at the Graphene−Water Interface. *Biomacromolecules* **2015**, *16* (6), 1771−1783.
(64) Paajanen, A.; Sonavane, Y.; Ignasiak, D.; Ketoja, J. A.; Maloney, T.; Paavilainen, S. Atomistic Molecular Dynamics Simulations on the Interaction of TEMPO-Oxidized Cellulose Nanofibrils in Water. *Cellulose* **2016**, *23* (6), 3449−3462.